Nano Research

Open Access

Research Article

Efficient water splitting with a MOF-74(Ni)-derived composite electrocatalyst prepared via microwave- and laser-assisted synthesis

Daria Givirovskaia[1] ✉, Georgy Givirovskiy[1] ✉, Ville Laitinen[1], Yuri Park[2], Parsa Amin[1], Aafaq ur Rehman[1], Nima Rezaei[1], and Eveliina Repo[1]

[1] *School of Engineering Science, LUT University, Lappeenranta 53850, Finland*
[2] *Institute of Environmental Technology, Seoul National University of Science and Technology, Seoul 01811, Republic of Korea*

Cite this article: *Nano Research*, **2025**, *18*, 94907100. https://doi.org/10.26599/NR.2025.94907100

ABSTRACT: Metal-organic frameworks (MOFs), with their highly coordinated structure, high porosity, and tunability have piqued vast scientific attention as a promising platform for creating high-efficiency electrocatalysts for water electrolysis. However, the conventional methods of creating MOF-derived electrocatalysts are time- and energy-consuming and often lead to significant aggregation of metal particles and the formation of non-homogeneous porous structures. In this research, we leverage the potential of the MOF-template-directed fabrication approach, combined with microwave heating and laser-assisted post-treatment, to develop a facile, scalable, and versatile strategy for electrocatalyst synthesis. Specifically, hierarchically structured Ni-based MOF-74 was rapidly synthesized from the Ni hydroxide nanosheet arrays deposited onto a Ni foam substrate using microwave-assisted synthesis. Subsequently, the obtained structures were treated using a focused laser to create MOF-74(Ni)-derived composite electrocatalyst featuring encapsulated nickel oxide nanoparticles. The resulting electrocatalyst exhibited high efficiency and stability for facilitating the oxygen evolution reaction (OER) under alkaline conditions. The outstanding electrocatalytic performance of the developed material enables it to reach a current density of 50 mA/cm^2 at an overpotential of 318 mV. High electrocatalytic activity can be attributed to its distinctive morphology, which offers numerous exposed active sites for water splitting. The experimental data gathered in this study is anticipated to be of significant value for the synthesis of other MOF-derived composite materials featuring hierarchical structures. Furthermore, the study emphasized the importance of using a combination of microwave heating and laser-assisted post-treatment of MOFs to achieve a sustainable and efficient process for electrocatalyst synthesis.

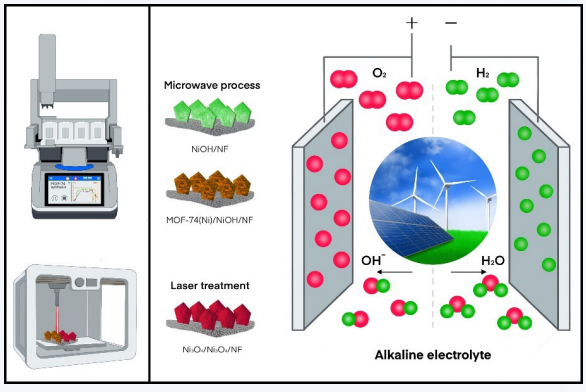

KEYWORDS: metal-organic framework, microwave-assisted synthesis, laser-assisted synthesis, nickel oxide nanoparticles, electrocatalysis

1 Introduction

Successfully transitioning from a fossil fuel-based economy to a renewable circular economy will lead to a society where fossil carbon-based goods and services are replaced by sustainable carbon sources [1–4]. As more countries pursue decarbonization strategies and transition towards zero carbon, H_2 will play a critical role in this transition as an energy carrier and as a raw material for producing carbon-neutral fuels and chemicals in Power-to-X processes [5–7]. The main synthesis pathway for the renewable H_2 production is through water electrolysis [8, 9], which is based on two fundamental electrochemical reactions: the hydrogen evolution reaction (HER) occurring at the cathode and the oxygen evolution reaction (OER) taking place at the anode [10]. The multi-electron and proton-coupled OER is a complex and kinetically slow reaction, and thus, requires a substantial energy input (large overpotentials) leading to the decreased energy efficiency of water electrolyzers [10–12]. To achieve reasonable water electrolysis efficiency and affordable H_2 production cost, noble-metal electrocatalysts and especially their oxides, such as IrO_2 and RuO_2, are widely used to catalyze thermodynamically unfavorable OER.

Received: August 23, 2024; **Revised:** September 29, 2024
Accepted: October 30, 2024

✉Address correspondence to Daria Givirovskaia, Daria.Givirovskaia@lut.fi; Georgy Givirovskiy, Georgy.Givirovskiy@lut.fi

Unfortunately, the exorbitant price and scarcity of Ru and Ir limit their practical applications and make them unsuitable for large-scale H_2 production [10, 13]. Thus, significant efforts have been dedicated to investigating non-noble metal electrocatalysts featuring high activity, stability, and low cost [14].

Over the past years, a number of different catalysts made of earth-abundant materials, such as transition metal (TM) oxides [15], hydroxides [16], sulfides [13], phosphates [17], borides [18], chalcogenides [19] are developed as promising substitutes for Ru and Ir. In this context of micro- and nano-material advancement, metal-organic frameworks (MOFs) have piqued vast scientific attention as a rapidly emerging research field with an increasing number of suggested applications [20, 21]. MOFs represent a new class of hybrid crystalline porous materials formed by organic linkers and metal ions, exhibiting remarkable characteristics such as: (i) exceptional surface area reaching 10,000 m^2/g, (ii) remarkably high porosity, (iii) homogeneous dispersion of open active centers, (iv) structural diversity, and (v) high degree of tunability [20, 22]. However, despite these advantageous properties and great potential, the direct application of MOF-based electrocatalysts for water electrolysis is postponed until the solution of inherent problems related to poor conductivity and instability in electrochemical systems [23]. Recent research findings indicate that the indirect use of MOFs as precursors and self-sacrificing templates for creating highly conductive nanostructured catalysts holds greater potential. Subjecting MOFs to high-temperature treatment under an inert gas atmosphere can transform them into the derived porous composite materials, as demonstrated by previous studies [24, 25]. These MOF-derived composites featuring encapsulated nanoparticles in their hierarchical structure exhibit abundant exposed active sites and high specific surface area which lead to high catalytic activity towards OER and HER.

It is well-established that the porosity and crystalline structure of MOFs and MOF-derived composites are known to be influenced by the conditions and techniques employed in the synthesis [26]. The most common synthesis strategy applied in the previously published research [24, 25] can be separated into two main steps: (i) the deposition of MOFs onto a conductive substrate through hydro- or solvothermal synthesis being performed in autoclaves, and (ii) the subsequent thermal treatment of the resulting MOF-based catalysts, either in the presence or absence of O_2. Notably, microwave-assisted synthesis can provide significant advantages over conventional hydro- or solvothermal methods, including (i) rapid volumetric heating, (ii) higher chemical reaction rates, leading to (iii) shorter reaction times, (iv) increased selectivity, (v) improved repeatability, and (vi) higher product yield [26, 27]. Furthermore, the significant benefit of microwave-assisted synthesis lies in its ability to fine-tune MOF properties like morphology, particle size, and phase by adjusting the applied power and reaction time [28, 29]. Previous studies have demonstrated that the synthesis under microwave irradiation often results in smaller crystal sizes due to the accelerated nucleation process [30–32]. The reduced MOF crystal size, particularly at the submicron- and nano-levels, is an advantage when developing high-activity water electrolysis catalysts [33].

The post-treatment of MOFs through heating is also a crucial step used to remove solvent molecules, enhance structural integrity, activate open metal sites, and improve stability [34, 35]. However, the conventional thermal treatment methods are time- and energy-consuming and usually require the use of an inert gas atmosphere. Moreover, during the conventional high-temperature treatment, the MOF particles tend to form agglomerates hindering the electron conductivity and impeding the efficient transport of reactants and products in electrocatalytic reactions [25]. In this context, the laser-induced treatment strategy offers advantages over conventional high-temperature post-treatment methods by preventing particle aggregation, reducing process time, and ensuring a high yield. The cost-effectiveness, precision, programmability, and scalability are other important benefits of the laser-induced post-treatment of MOFs [36].

Despite the advantages described above, only a few reports have explored the use of laser-treated MOFs in water-splitting applications [37, 38]. Furthermore, to the best of our knowledge, there are no studies where the microwave-assisted synthesis of MOFs is followed by laser-assisted conversion to porous composite electrocatalysts. This study investigated the potential to enhance water electrolysis efficiency by combining the unique advantages of hierarchically structured MOF-derived electrocatalysts, utilizing microwave-assisted synthesis, and employing laser-induced post-treatment in one process. MOF template-directed strategy was applied to grow MOF-74(Ni) from the corresponding NiOH nanostructures onto a conductive nickel foam (NF) substrate with a high surface area and under microwave irradiation. Subsequently, a focused laser was used for MOF-74(Ni) post-treatment under ambient conditions to create an efficient electrocatalyst with extensive exposed active sites and enhanced conductivity provided by its distinctive morphology. This study emphasizes the potential of integrating microwave- and laser-assisted technologies to establish a sustainable, cost-effective, and scalable strategy to develop highly efficient MOF-derived electrocatalysts.

2 Experimental

2.1 Materials

All chemical reagents used in the experimental work were acquired from Sigma-Aldrich, USA, and utilized without pretreatment unless otherwise specified. Noble-metal IrO_2/Ti and Pt/Ti electrodes were purchased from PV3 Technologies, UK. The reference electrode (Hg/HgO) was purchased from C3 Prozess- und Analysentechnik GmbH, Germany. NF (purity: 99.8%, porosity: 97%, thickness: 2 mm, PPI: 110) was obtained from Tmax Battery Equipments Limited Company, China.

2.2 Catalyst fabrication

The catalyst synthesis procedure is outlined in Fig. 1. In this study, NF was selected as the substrate for catalyst deposition due to its relatively high electron conductivity, large surface area, and affordability. Before the deposition process, the NF substrates underwent a thorough cleaning sequence involving 10 min of ultrasound treatment in acetone, absolute ethanol, and 3 M HCl each. Following the removal of surface pollutants and the oxide layer, the NF substrates were rinsed in deionized water and subsequently dried at room temperature, preparing them for the catalyst deposition.

The first deposition step involved coating the NF substrates with NiOH nanosheet arrays, serving as the self-sacrificing templates for the subsequent synthesis of MOF-74(Ni). The precursor solution for NiOH catalyst fabrication consisted of 0.05 M $Ni(NO_3)_2{\cdot}6H_2O$ and 0.1 M urea. The reaction solution, combined with the NF substrates, was exposed to microwave radiation at a maximum power of 150 W and heated to 200 °C for 0.5 h using a microwave

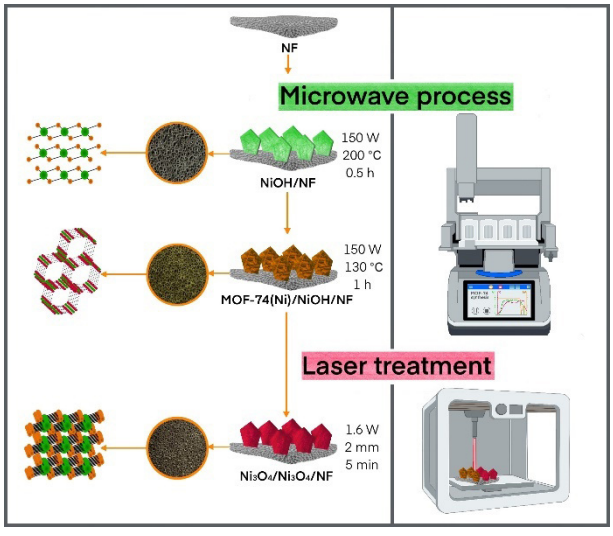

Figure 1 Schematic illustration of the microwave- and laser-assisted synthesis of a MOF-74(Ni)-derived composite electrocatalyst featuring encapsulated Ni_3O_4 nanoparticles.

reactor (Discover 2.0, CEM Corporation). After microwave-assisted synthesis, the NiOH/NF samples were rinsed in absolute ethanol and deionized water and dried at 50 °C overnight to remove the absorbed solvents.

The second synthesis step involved the *in-situ* growth of MOF-74(Ni) on top of NiOH/NF. To achieve this, the as-prepared NiOH/NF samples were transferred to a solution containing 25 mL of N,N-dimethylformamide (DMF), 2.5 mL of deionized water, 2.5 mL of absolute ethanol, and 0.1 g of 2,5-dihydroxyterephthalic acid. The solution was exposed to microwave radiation at a maximum power of 150 W and heated to 130 °C for 1 h. Following microwave-assisted growth, the resulting MOF-74(Ni)/NiOH/NF samples were thoroughly washed in absolute ethanol and deionized water, then dried at 85 °C for 12 h.

The final step in catalyst fabrication involved the post-treatment of MOF-74(Ni)/NiOH/NF with a 1.6 W laser using a Snapmaker A350T. The laser treatment program was created using Snapmaker's third-party software, adjusting the operating parameters such as a fill interval of 0.05 mm, a work speed of 500 mm/min, and the laser power setting. The samples were treated under ambient conditions with a laser power of 1.6 W, a wavelength of 405 nm, and a distance of 2 mm between the laser and the sample, applied from both sides. Following the laser-assisted post-treatment, the resulting samples, denoted as Ni_3O_4/Ni_3O_4/NF, underwent ultrasonication in ethanol to remove any surface pollutants before being dried overnight in a convection oven at 50 °C.

2.3 Material characterization

All synthesized samples were characterized using the following methods. A Hitachi S-3400N field-emission scanning electron microscope (FE-SEM) with energy-dispersive X-ray spectroscopy (EDX) was employed to analyze the surface morphology and elemental composition distribution of the synthesized catalysts. SEM images were captured at 10 kV and 20 mA using both an UDV (secondary electron detector) and a BSE (backscatter electron detector). EDX peaks were obtained at 20 kV and 40 mA. The crystal structure of the catalysts was analyzed by X-ray diffraction (XRD). XRD analysis was conducted using a PANalytical Empyrean 3 diffractometer equipped with a PIXcel3D-Medipix3 detector, a Si zero background powder holder, and poly-capillary optics for precise beam control (slit-controlled beam size: height of 1 mm and width of 8 mm). The tube settings employed were 30 kV and 30 mA. To identify the functional groups and investigate the presence of anions, which may be incorporated in the interlayers of catalysts, Fourier-transform infrared spectroscopy (FT-IR) analysis was performed. FT-IR analysis was conducted on PerkinElmer Inc. spectrometer equipped with the universal diamond crystal ATR module over the range of 400–4000 cm^{-1}. In the thermogravimetric analysis (TGA), approximately 5 ± 0.1 mg of the sample was subjected to heating from 25 to 900 °C at a rate of 10 °C/min. This process was conducted under a nitrogen atmosphere, utilizing a flow rate of 40 mL/min of nitrogen, facilitated by a NETZSCH STA 449C instrument. Micromeritics 3Flex was used to determine the specific surface area and pore size distribution of as-prepared catalysts by the Brunauer–Emmett–Teller (BET) and Barrett–Joyner–Halenda (BJH) methods, respectively. X-ray photoelectron spectrometer (XPS) (Nexsa, Thermo Fisher Scientific Brno s.r.o, Czech Republic) equipped with a monochromated Al X-ray source (Al Kα line: 1486.6 eV) was applied to verify the surface elemental composition of the synthesized materials. The Agilent Technologies 7900 was used to perform inductively coupled plasma mass spectrometry (ICP-MS) measurements of the 1 M KOH electrolyte after the electrolysis tests.

2.4 Electrochemical measurements

The electrochemical measurements were conducted with the Autolab PGSTAT302N Potentiostat from Metrohm, Switzerland, in the three-electrode system configuration at room temperature. As-prepared catalysts and IrO_2/Ti were employed as the working electrodes (WE). Pt/Ti was utilized as the counter electrode (CE), while a Hg/HgO electrode (1 M KOH) served as the reference electrode (RE). Polarization curves were measured using linear sweep voltammetry (LSV) at a scan rate of 5 mV/s in 1 M KOH. The Tafel slope, a crucial representative parameter in the assessment of OER kinetics, was calculated based on the obtained LSV curves. Catalyst long-term stability assessments were conducted via chronopotentiometry for 36 h at a constant current density maintained at 10, 50, and 100 mA/cm. The electrochemically active surface area (ECSA) is proportional to the double-layer capacitance (C_{dl}), which was calculated from cyclic voltammetry curves measured at scan rates of 2, 4, 6, 8, and 10 mV/s in the non-Faradaic region of 1.1–1.15 V. The half of the difference between the anodic (I_a) and the cathodic (I_c) charging currents at the midpoint of the potential window (1.125 V) was plotted against the corresponding scan rates. This plot exhibits a linear relationship, and its slope represents the C_{dl} value. The electrochemical impedance spectroscopy (EIS) measurements were performed across a frequency range of 100 kHz to 10 mHz, using an overpotential of 300 mV for OER. In this study, all potentials were calibrated to a reversible hydrogen electrode (RHE) using the provided equation [39]

$$E_{RHE} = E_{Hg/HgO} + 0.1053V + 0.059pH \quad (1)$$

3 Results and discussion

3.1 Catalyst synthesis

During microwave heating, the microwave directly interacts with

the solvent molecules, leading to a rapid temperature increase in the reaction media and localized superheating. This unique feature of microwave-assisted synthesis minimizes the wall effect commonly experienced in conventional heating methods [27]. By facilitating rapid and energy-efficient heat transfer to the reactants, chemical reactions undergo accelerated kinetics, resulting in reduced reaction times and the formation of finer particles, typically on a nano-sized scale [31]. In the context of water electrolysis, nano-sized catalysts play a pivotal role in enhancing the process efficiency. The increased surface area of these catalysts, combined with their tailored properties, promotes OER and HER, efficient mass transport, and lower overpotentials [40].

In this study, microwave-assisted synthesis was employed to reduce the reaction time and achieve a distinctive nano-sized morphology for the hierarchically structured composites. Following the step-by-step synthesis procedure, the NF substrate was initially coated with NiOH nanosheet arrays (Fig. 2(b)), requiring a 0.5 h reaction time. The resulting NiOH/NF exhibited an average pore size of 6–7 nm, as determined by BET/BJH analysis. For comparison, in the study by Yi et al. [41], utilizing the same synthesis temperature as our study (200 °C), flower-like nanostructured NiOH was grown on NF in an autoclave with a reaction time of 12 h, resulting in an average pore size of 14 nm. In another study by Cao et al. [42], the synthesis time for similar NiOH nanoplates was 4–6 h, with an average particle size of 60–90 nm. Hence, the use of microwave-assisted synthesis not only significantly reduces the synthesis time of NiOH, by approximately 24 times less compared to the study of Yi et al. [41], but also results in a substantial decrease in the average pore size, approximately 10–13 times smaller compared to the study by Cao et al. [42].

Subsequently, the microwave-assisted method was employed to synthesize MOF-74(Ni)/NiOH/NF (Fig. 2(c)). The application of microwave heating is particularly justified for solvents with large dipole moments, low thermal conductivity, and relatively short relaxation times, such as DMF [31], which was used in this study. The synthesis required only 1 h, yielding MOF-74(Ni) with an average pore size of 4–5 nm as determined by BET analysis. In contrast, conventional solvothermal synthesis, as observed in the studies by Nakatsuka et al. [43] and Chen et al. [44], required a much longer reaction time of 24 h. Chen et al. [44] achieved MOF-74 structures composed of nanoparticles with an average size of 10 nm, as determined by TEM analysis, which is still twice the size obtained in our research. Therefore, microwave-assisted synthesis provides significant advantages over conventional solvothermal synthesis for the rapid fabrication of MOF-74(Ni) using DMF as a solvent.

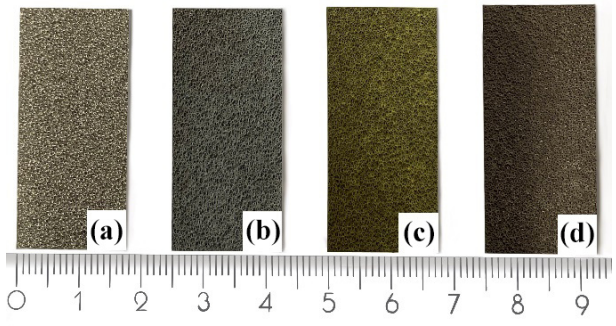

Figure 2 Photos of electrode surface changes: (a) bare NF, (b) NiOH/NF, (c) MOF-74(Ni)/NiOH/NF, and (d) Ni_3O_4/Ni_3O_4/NF during step-by-step preparation of hierarchically-structured composite electrocatalyst.

As mentioned earlier, conventional thermal treatment processes of MOFs for electrocatalysis demand elevated temperatures, inert atmospheres, and prolonged durations. To provide a more efficient alternative, the final synthesis step involved treating MOF-74(Ni)/NiOH/NF with a laser. This process required only 15 min to treat the surface area of 10 cm^2. In contrast, conventional post-treatments of MOF structures typically involve heating for 2–3 h at 350–400 °C [24, 25, 43]. Moreover, conventional thermal post-treatment of MOFs has been associated with particle aggregation [37]. However, our SEM analysis (Fig. 3(d)) revealed no significant particle aggregation on the resulting Ni_3O_4/Ni_3O_4/NF. This indicates that the synergistic use of microwave and laser-assisted approaches not only results in a significantly faster preparation of hierarchically structured MOF-derived catalysts but also mitigates issues such as particle aggregation. These advantages contribute to environmentally friendly practices by reducing the overall energy consumption and waste generation.

3.2 Physical characterization

The surface morphology of the synthesized catalysts was investigated using SEM as illustrated in Fig. 3. Following the detailed synthesis procedure outlined in Section 2.2, the NF substrate was initially coated with NiOH (Fig. 3(a)). The SEM images reveal that the surface morphology of the as-prepared NiOH/NF is comprised of nanosheet arrays with excellent alignment, vertical growth, and a high surface-to-volume ratio. The NiOH/NF coating served a dual role: firstly, as self-sacrificial precursor and source of Ni ions, and secondly, as a structural framework for the formation of MOF-74(Ni)/NiOH/NF (Fig. 3(b)). According to the low- and high-magnification SEM images, the surface of MOF-74(Ni)/NiOH/NF is highly rich in macroporosity, consisting of micro-rods with rice-like shapes. These particles grew on top of NiOH nanosheets, exhibiting the hierarchical structure inherited from hydroxide arrays by MOF-74(Ni). Laser treatment led to the cleaning of the catalyst surface from residual solvents and the elimination of weakly bounded structures. The resulting Ni_3O_4/Ni_3O_4/NF morphology exhibited nano-sized particles being homogeneously distributed on the nanosheet array skeleton (Fig. 3(c)).

The EDX spectra of the as-prepared NiOH/NF, MOF-74(Ni)/NiOH/NF, and Ni_3O_4/Ni_3O_4/NF electrocatalysts are presented in Fig. 4(a). The presence of Ni, O, and C can be confirmed by examining the corresponding peaks in the EDX diagrams. Notably, the EDX mapping diagrams (Fig. 3(d)) revealed a uniform distribution of Ni, O, and C throughout the electrocatalysts, underscoring the successful synthesis process. Furthermore, through quantitative EDX analysis, the weight percentage changes for the respective elements at each synthesis step were assessed, with summarized results presented in Table 1. The observed significant reduction in carbon content following laser treatment of MOF-74(Ni) clearly highlights the degradation of the organic linker during the thermal treatment process.

The XRD analysis aimed to evaluate the crystallinity of the prepared samples and confirm the presence of the desired structures. As shown in Fig. 4(b), strong diffraction peaks observed in all catalysts at 44.5° and 52.2° correspond to the NF substrate. The characteristic diffraction peaks for NiOH appeared at 2θ = 19.7°, 33.1°, 38.8°, and 59.2°, corresponding to the (001), (100), (101), and (110) planes, respectively [45]. Following the synthesis of MOF-74(Ni)/NiOH/NF, notable diffraction peaks emerged at 2θ = 6.8° and 11.9°, aligning with the (210) and (300) crystallographic

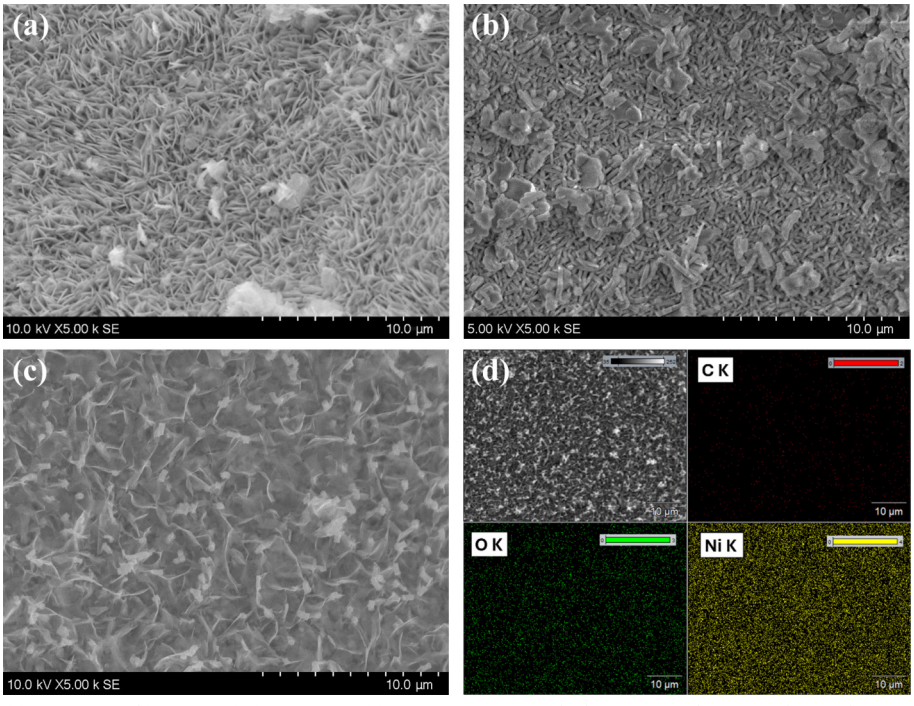

Figure 3 SEM images of (a) NiOH/NF, (b) MOF-74(Ni)/NiOH/NF, (c) Ni_3O_4/ Ni_3O_4/NF, (d) the corresponding EDS elemental mapping of the resulting Ni_3O_4/Ni_3O_4/NF composite.

planes for MOF-74(Ni) [46]. Interestingly, the intensity of MOF-74(Ni) peaks decreased upon laser treatment, suggesting its structural transformation and degradation. New peaks appeared at around 2θ = 37.4° and 43.3°, indexed as (111) and (200) planes of NiO [43]. In this study, the diffraction peaks of NiOH/NF, MOF-74(Ni)/NiOH/NF, and Ni_3O_4/Ni_3O_4/NF were matched against the corresponding powder diffraction files (PDFs), including PDF 04-012-5845, PDF 00-065-0862, and PDF 00-004-0835. The observed differences in the peak width and relative intensity are related to the structural defects, differences in the level of crystallization, and the decrease in the crystallite size [46].

The bonding and chemical information of the as-prepared catalysts were investigated using FT-IR spectroscopy, as illustrated in Fig. 4(c). Analysis of FT-IR spectra reveals the presence of NiOH, which is evident from the characteristic peak at 521 cm^{-1}, indicating Ni–O–H bending and Ni–O stretching vibrations. The peak observed at 1632 cm^{-1} corresponds to the bending vibration of the absorbed H_2O molecule [47]. Additionally, a sharp peak at 3640 cm^{-1} corresponds to the stretching vibration of the free OH group which confirms the successful formation of $Ni(OH)_2$ [48]. Consistent with prior research [30], the characteristic FT-IR peaks of MOF-74(Ni) were identified at wavenumbers of 1560, 1411, 1360, 1243, 1199, 1124, 887, 825, 633, and 588 cm^{-1}. After laser treatment, the intensity of MOF-74(Ni) peaks decreased drastically, suggesting significant structural changes in the resulting composite material. In the FT-IR spectra of Ni_3O_4/Ni_3O_4/NF, the sharp peak observed at 447 can be attributed to Ni–O stretching vibration, confirming successful dehydration of Ni(OH) upon laser treatment and the formation of NiO [48, 49].

The thermal stability of the samples was analyzed through thermogravimetric analysis (TGA). As depicted in Fig. 4(d), the initial weight loss, attributed to the moisture evaporation, occurred in the temperature range of 25–100 °C. Subsequently, significant weight loss was observed between 200–450 °C, indicating a gradual release of the volatile components in all samples. Based on the obtained results, the thermal stability of the investigated catalysts followed the order: NiOH/NF > Ni_3O_4/Ni_3O_4/NF > MOF-74(Ni)/NiOH/NF. Notably, MOF-74(Ni)/NiOH/NF exhibited the most substantial weight loss, suggesting lower thermal stability compared to the other porous materials. The laser treatment process appears to influence the thermal behavior of the resulting Ni_3O_4/Ni_3O_4/NF, potentially contributing to material stabilization and mitigating its decomposition mechanism.

The surface area and pore size distribution of the synthesized catalysts were investigated using N_2 adsorption–desorption isotherms, analyzed with the BET and BJH methods, respectively. The pore size analysis, presented in Fig. 4(e), reveals that all the catalysts predominantly consist of mesopores, with the majority of the pores ranging from 2 to 5 nm. From the N_2 adsorption-desorption isotherm depicted in Fig. 4(f), the BET surface areas of NiOH/NF, MOF-74(Ni)/NiOH/NF, and Ni_3O_4/Ni_3O_4/NF were calculated to be 6.68, 31.76, and 14.83 m^2/g, respectively. The measured BET surface areas of NiOH/NF and MOF-74(Ni)/NiOH/NF are substantially smaller compared to similar materials previously reported [30, 41]. These differences in BET surface area measurements may be attributed to the influence of the NF substrate mass, as the calculated BET values represent the surface area per mass of the entire electrode, rather than solely per mass of the deposited catalyst. Nevertheless, the BET surface area of the resulting Ni_3O_4/Ni_3O_4/NF is comparable to those of previously reported MOF-derived catalysts after laser treatment [37], likely because the BET measurements were conducted in a similar manner, considering the mass of the entire electrode.

The oxidation state and binding characteristics of the metal ions in the synthesized catalysts were investigated through XPS analysis. Figure 5 shows the XPS spectra for the NiOH/NF, MOF-74(Ni)/NiOH/NF, and Ni_3O_4/Ni_3O_4/NF electrocatalysts. The deconvoluted peaks in the Ni 2p region for all investigated materials

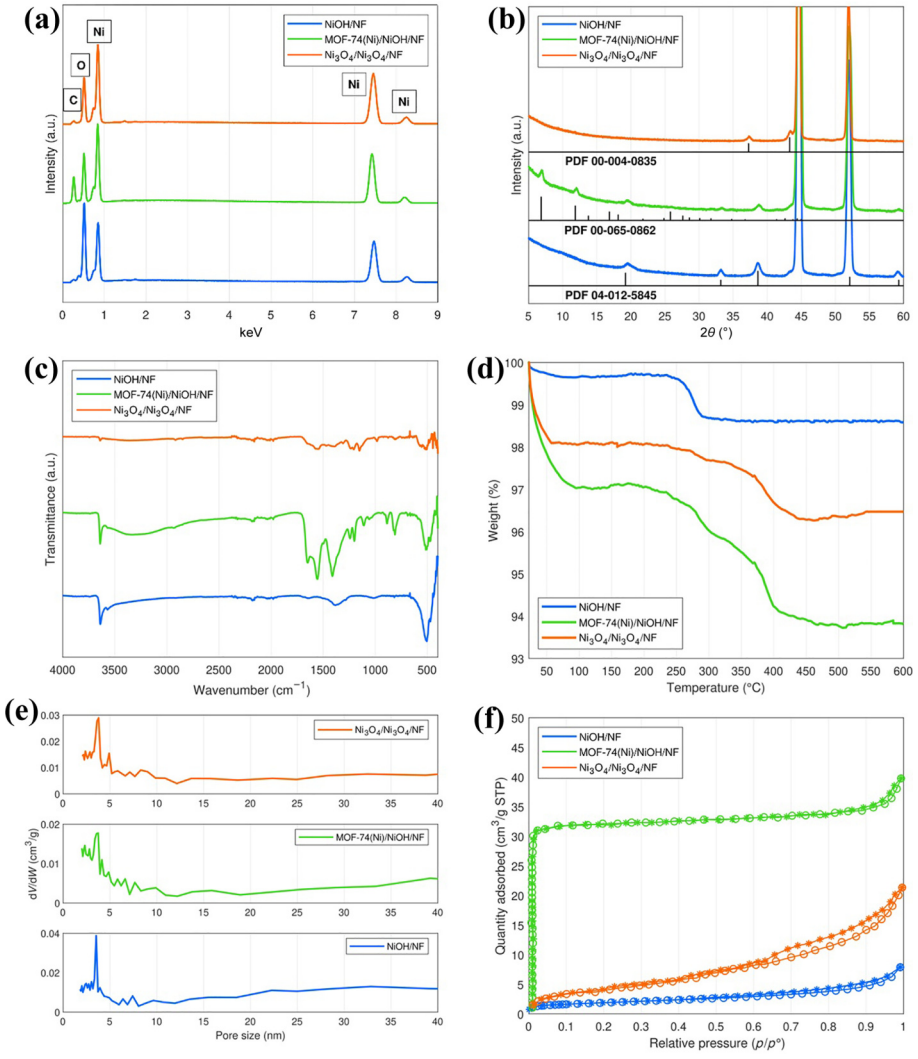

Figure 4 Physical characterization of investigated catalysts: (a) EDX spectra, (b) XRD patterns, (c) FT-IR spectra, (d) TGA curves, (e) pore-size distribution, and (f) N_2 adsorption–desorption isotherms.

Table 1 Weight percentages of Ni, O, and C elements in NiOH/NF, MOF-74(Ni)/NiOH/NF, and Ni_3O_4/Ni_3O_4/NF electrocatalysts as determined by quantitative EDX analysis

Catalyst	Ni (%)	O (%)	C (%)
NiOH/NF	72.10	26.26	1.65
MOF-74(Ni)/NiOH/NF	62.09	15.14	22.77
Ni_3O_4/Ni_3O_4/NF	83.88	13.31	2.81

are presented in Figs. 5(b)–5(d). In Fig. 5(b), distinct peaks at 856.5 and 874.2 eV were observed for NiOH/NF, corresponding to Ni^{3+} ions [50]. Similarly, MOF-74(Ni)/NiOH/NF displayed slightly shifted peaks at approximately 856.1 and 873.9 eV, also indicative of Ni^{3+} ions [44]. After laser treatment, Ni_3O_4/Ni_3O_4/NF exhibited the co-existence of Ni^{2+} (853.9 and 861.1 eV) and Ni^{3+} (855.7 and 873.2 eV) ions, as evidenced by the deconvoluted peaks presented in Fig. 5(d) [43, 50, 51].

Figures 5(e) and 5(f) present the O 1s and C 1s spectra for the NiOH/NF, MOF-74(Ni)/NiOH/NF, and Ni_3O_4/Ni_3O_4/NF, respectively. The deconvoluted O 1s spectrum of NiOH/NF displayed a prominent peak centered around 531.3 eV, corresponding to bound –OH groups, and a smaller peak near 534.4 eV, attributed to organic contamination [50, 52]. The high-resolution O 1s XPS spectra of MOF-74(Ni)/NiOH/NF exhibited peaks at 531.3, 532.2, and 533.5 eV, indicating the presence of –OH, C=O, and C–OH groups, respectively [53]. The O 1s spectra for the resulting Ni_3O_4/Ni_3O_4/NF contained two main peaks centered at 529.4 and 531.3 eV, corresponding to M–O bonds and adsorbed –OH groups, respectively [44, 50]. The presence of the M–O bond confirms the surface oxidation of Ni during the laser treatment under ambient conditions.

As shown in Fig. 5(f), the high-resolution C 1s spectra of NiOH/NF exhibit four deconvoluted peaks at 284.7, 285.2, 286.4, and 287.5 eV, corresponding to C=C, C–C, C–OH, and C=O groups [54]. In the high-resolution C 1s spectra of MOF-74(Ni)/NiOH/NF, peaks at approximately 284.8, 286.4, and 288.4 eV are attributed to C=C, C–OH, and O–C=O groups [50]. After laser treatment, Ni_3O_4/Ni_3O_4/NF showed peaks centered at 285.1, 286.7, and 288.7 eV, characteristic of C–C, C–O, and C=O groups, respectively [53].

3.3 Catalytic activity

The OER activity of Ni_3O_4/Ni_3O_4/NF was evaluated in a 1 M KOH solution using a conventional three-electrode electrochemical cell

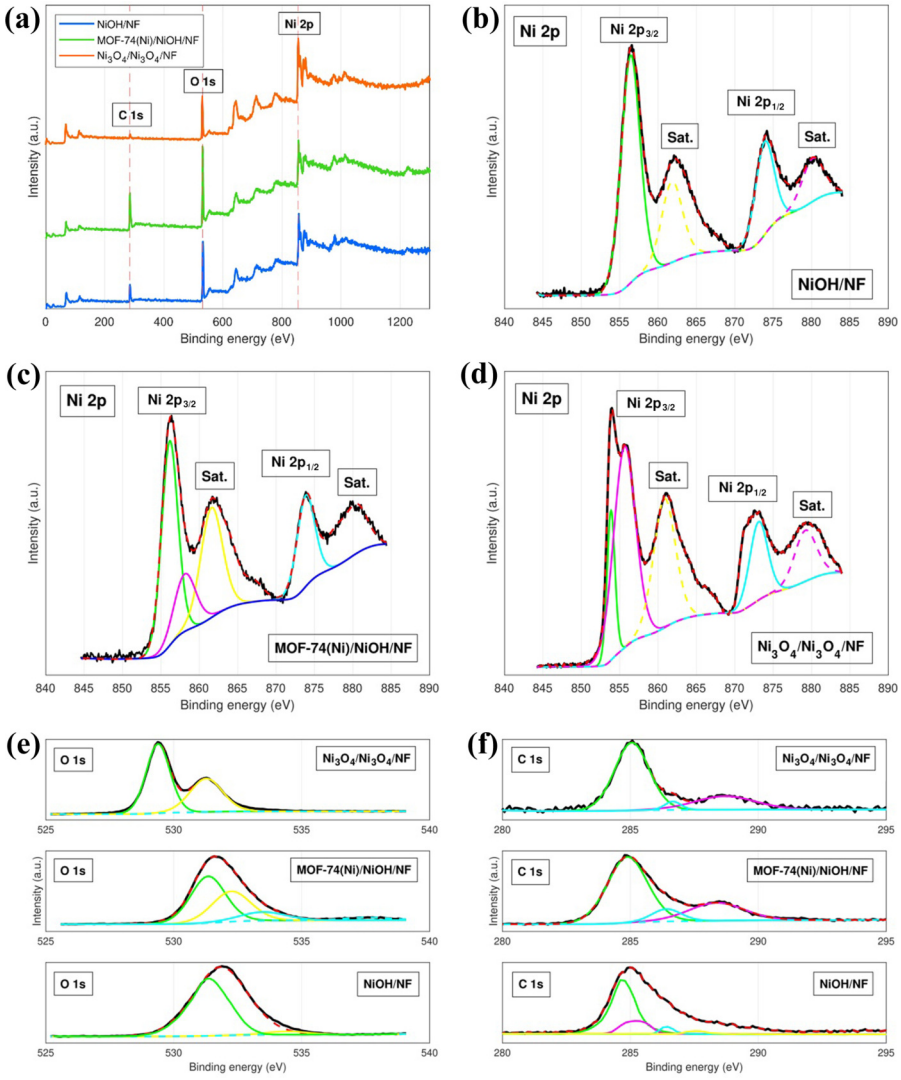

Figure 5 (a) XPS survey, high-magnification XPS spectra in the Ni 2p region for (b) NiOH/NF, (c) MOF-74(Ni)/NiOH/NF, and (d) Ni_3O_4/ Ni_3O_4/NF, and the corresponding spectra in the (e) O 1s and (f) C 1s regions for all investigated materials.

operated at room temperature. Commercial IrO_2, NF, and as-prepared NiOH/NF electrodes were used as reference anode materials for comparison of OER activity. Current density measurements were obtained as a function of cell voltages via LSV at a scan rate of 5 mV/s, as illustrated in Fig. 6(a). The LSV measurements revealed that the onset potential of Ni_3O_4/Ni_3O_4/NF was approximately 1.39 V, indicated by a sharp increase in current density beyond this potential. In contrast, the onset potential of commercial IrO_2 was notably higher, around 1.52 V. Figure 6(b) demonstrates overpotentials required to reach reference current densities of 10 and 50 mA/cm^2 by the investigated catalysts. To achieve a current density of 10 mA/cm^2, Ni_3O_4/Ni_3O_4/NF required an overpotential of approximately 205 mV, resulting in reductions of 46, 153, and 165 mV compared to NiOH/NF, NF, and IrO_2, respectively. This difference in the activity was further emphasized when targeting a substantially higher current density of 50 mA/cm^2. Hierarchically structured Ni_3O_4/Ni_3O_4/NF demonstrated an overpotential of 318 mV to achieve 50 mA/cm^2, representing reductions of almost 179, 209, and 235 mV compared to NiOH/NF, NF, and IrO_2, respectively.

The significant difference in the OER activity between Ni_3O_4/Ni_3O_4/NF and benchmark IrO_2 used in this study can be partly attributed to the contrasting nature of their substrates. NF offers a highly porous and three-dimensional structure, which provides a substantial increase in the electrochemically active surface area compared to the relatively flat Ti plates used for commercial IrO_2 deposition. The enhanced surface area of NF substrate supports a greater density of active sites, facilitating more efficient electron transfer and improved mass transport, making the direct comparison of electrocatalysts deposited on NF with those on flat surface electrodes somewhat inequitable.

To provide context, a recently published study by Milazzo et al. [55] indicates that IrO_x deposited on NF required an overpotential of 360 mV to achieve a current density of 10 mA/cm^2, which is 10 mV lower than the overpotential required for IrO_2/Ti in our study. Zhou et al. [24] used an Ir/C catalyst that exhibited an overpotential of 310 mV at 10 mA/cm^2. Liu et al. [56] reported a self-supported hierarchical nanocomposite IrO_2/NiO-based porous electrocatalyst deposited on NF, capable of reaching 10 mA/cm^2 at an overpotential of 278 mV. Interestingly, at a reference current density of 10 mA/cm^2, the Ni_3O_4/Ni_3O_4/NF developed in this study required 73 mV less overpotential than the IrO_2/NiO/NF developed

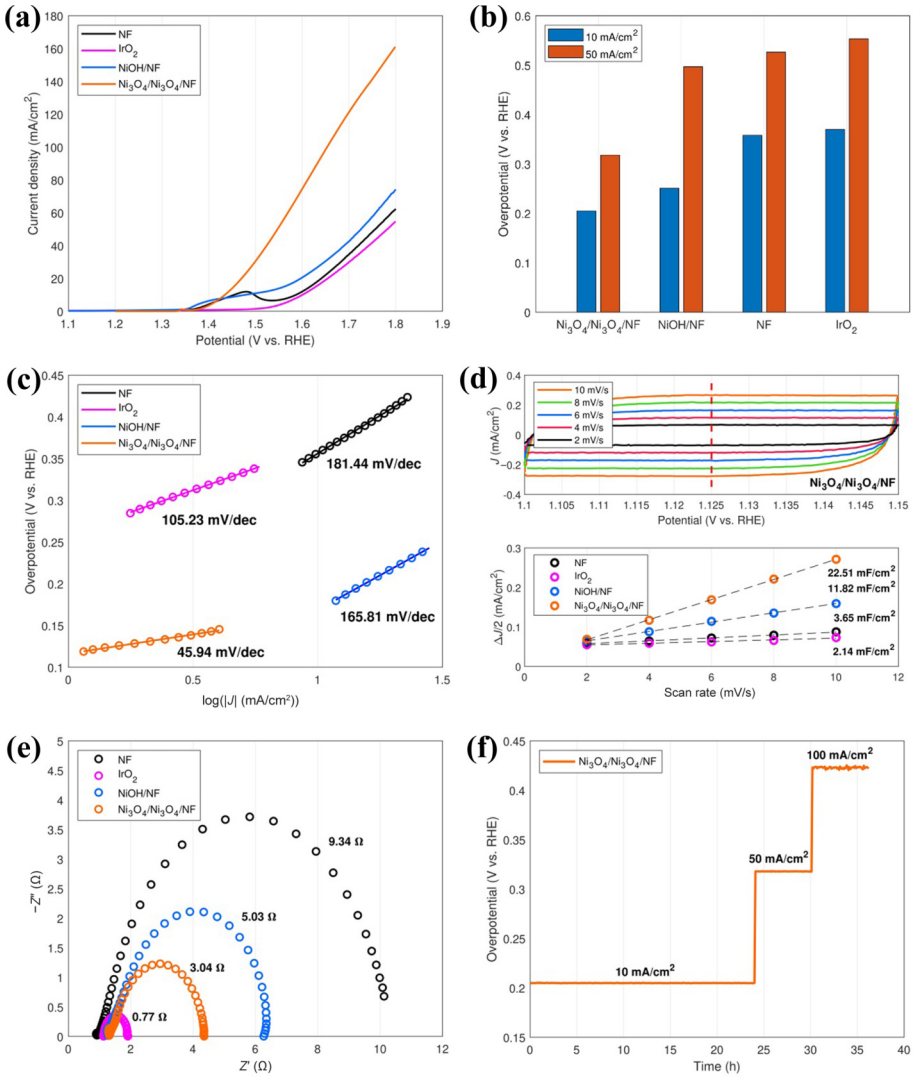

Figure 6 Electrocatalytic performance of investigated catalysts for OER in 1 M KOH: (a) LSV polarization curves, (b) overpotentials at 10 and 50 mA/cm^2, (c) Tafel plots, (d) results of C_{dl} measurements, (e) EIS spectra, and (f) chronopotentiometric curves at 10, 50, and 100 mA/cm^2 over 36 h for Ni_3O_4/Ni_3O_4/NF.

by Liu et al. [56], despite the presence of precious Ir and certain similarities in the hierarchical design of both materials. To further highlight the superior performance and efficiency of the developed catalyst, Table 2 summarizes the OER performance of the Ni_3O_4/Ni_3O_4/NF compared with other recently published hierarchically structured catalysts.

The Tafel slope is an essential representative parameter for the evaluation of OER kinetics. Tafel slopes of the investigated electrocatalysts were determined from the data shown in Fig. 6(c). Among all tested catalysts, Ni_3O_4/Ni_3O_4/NF exhibited the lowest Tafel slope, approximately 46 mV/dec, which is consistent with the second electron transfer step in the OER mechanism being the rate-determining step [10, 61]. The observed Tafel slope for Ni_3O_4/Ni_3O_4/NF is lower than those reported for previously published MOF-derived composites [24, 25]. In contrast, other tested catalysts exhibited relatively high Tafel slopes, close to or higher than 120 mV/dec, indicating a comparatively slow OER kinetics characterized by the adsorption and discharge of OH^- ions as the reaction rate-determining step [10, 62].

The ECSA, a crucial metric indicating the number of active sites on a catalyst's surface, can be estimated using the C_{dl} measured in a non-Faradaic region. As shown in Fig. 6(d), the calculated C_{dl} for the Ni_3O_4/Ni_3O_4/NF electrocatalyst is 22.51 mF/cm^2. Other tested

Table 2 Comparison of the overpotentials (η) at 10 mA/cm^2 and Tafel slopes of the developed Ni_3O_4/Ni_3O_4/NF with recently reported hierarchically structured electrocatalysts for OER in 1 M KOH

Catalyst	η (mV)	Tafel slope (mV/dec)	Ref.
Ni_3O_4/Ni_3O_4/NF	205	46	This work
Co_3O_4/Co_3O_4/Ni foil	301	115.3	[24]
CoS/Co_3O_4/Ni foil	289	77.6	[24]
C/Co_3O_4/Ni foil	261	65.4	[24]
CoP/Co_3O_4/Ni foil	238	51.4	[24]
CoNC/CoO/NF	309	53	[25]
IrO_x/NF	360	38	[55]
IrO_2/NiO/NF	278	41.8	[56]
$CoSe_2$/C fiber	297	41	[57]
NiFeMo/NF	238	35	[58]
NiFeCo-LDH/C fiber	249	42	[59]
$MnCo_2O_4/Ni_2P$/NF	240	114	[60]

catalysts showed substantially lower values of C_{dl}, specifically 2.14, 3.65, and 11.82 mF/cm^2, for IrO_2, NF, and NiOH/NF, respectively. Since ECSA is directly proportional to the C_{dl}, the obtained value confirms the presence of abundant exposed active sites in the Ni_3O_4/Ni_3O_4/NF, which is slightly higher compared to previously published hierarchically structured materials [24].

To analyze the charge transport kinetics between the developed Ni_3O_4/Ni_3O_4/NF and the electrolyte, EIS measurements were conducted at an overpotential of 300 mV. Using the Nyquist plot presented in Fig. 6(e), the charge transfer resistance (R_{ct}) values were calculated as 9.34, 5.03, 3.04, and 0.77 Ω, respectively, for NF, NiOH/NF, Ni_3O_4/Ni_3O_4/NF, and IrO_2. Although the R_{ct} of Ni_3O_4/Ni_3O_4/NF is slightly higher compared to the benchmark IrO_2, the developed catalyst still demonstrates efficient charge transport kinetics [24]. It is important to note that charge transfer resistance is only one of several factors influencing the overall OER performance, with other factors such as active site density, intrinsic catalytic activity and stability (Fig. 7) also playing crucial roles.

As previously mentioned, stability is another crucial parameter when assessing the catalyst performance in practical applications. In Fig. 6(d), the chronopotentiometric curves of Ni_3O_4/Ni_3O_4/NF are depicted, showing measurements at reference current densities of 10, 50, and 100 mA/cm^2 over 36 h of water electrolysis tests in a 1 M KOH solution. The results indicate that the Ni_3O_4/Ni_3O_4/NF catalyst has consistently maintained a relatively stable potential

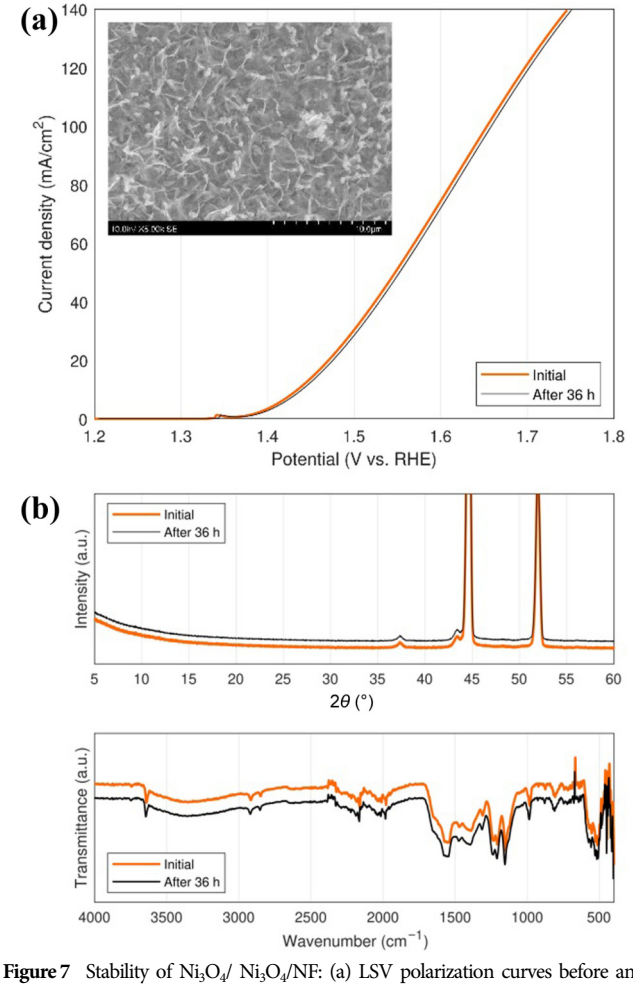

Figure 7 Stability of Ni_3O_4/ Ni_3O_4/NF: (a) LSV polarization curves before and after 36 h of water electrolysis tests. The inset in (a) shows the SEM image of the catalyst surface after stability testing. (b) Corresponding XRD and FT-IR patterns.

throughout the water-splitting process. Only a minor increase in potential, by approximately 1.5%, was observed when maintaining the current density at 100 mA/cm^2. This slight potential increase can be partly attributed to the formation of bubbles on the electrode surface under vigorous O_2 evolution. The ICP analysis revealed a Ni content of 0.674 μg/L in the 1 M KOH solution following the water electrolysis test, suggesting no significant leaching of the catalyst during stability studies. Additionally, SEM, XRD, and FT-IR analyses were conducted to investigate possible structural changes in the electrocatalyst after the stability tests, but no significant alteration was detected (Fig. 7). A minor decrease in intensities and slight shifts in the locations of peaks were observed in the FT-IR spectrum. The results suggest that the as-prepared Ni_3O_4/Ni_3O_4/NF catalyst is highly stable, presumably due to its robust structure and good catalyst adhesion to the NF substrate.

4 Conclusions

This study presents an innovative approach for the rapid synthesis of MOF-74(Ni)-derived composite electrocatalyst featuring encapsulated Ni_3O_4 nanoparticles, using the advantages of microwave- and laser-assisted technologies. By integrating these techniques, the synthesis time is significantly reduced compared to conventional methods, while ensuring the formation of a highly structured catalyst surface with uniformly distributed nanoparticles. The resulting electrocatalyst exhibits a remarkable OER performance, surpassing that of the commercial precious IrO_2. Notably, the catalyst demonstrates an overpotential of only 318 mV at 50 mA/cm^2, a small Tafel slope of around 46 mV/dec, and excellent long-term stability in 1 M KOH. This superior activity is attributed to the unique hierarchical structure of the catalyst, facilitating a large surface area, abundant active sites, and rapid electron transfer. The proposed synthesis strategy holds promise for the development of other hierarchically structured MOF-derived catalysts for applications in energy conversion and storage.

Data availability

All data needed to support the conclusions in the paper are presented in the manuscript and the Electronic Supplementary Material. Additional data related to this paper may be requested from the corresponding author upon request.

Acknowledgements

The authors are grateful for support from the European Regional Development Fund (Regional Council of Etelä-Karjala, project codes A77605 and 401320), the Academy of Finland (project code: 330076), and the AMBI (Analytics-based Management for Business and Manufacturing Industry) research platform of Lappeenranta-Lahti University of Technology LUT. The authors also acknowledge the assistance of the staff from the Jamie Hyneman Center (JHC) at LUT and LAB student Ivan Telmanov for his support with the experimental work in this study.

Declaration of competing interest

All the contributing authors report no conflict of interests in this work.

Author contribution statement

D. G.: Data curation, investigation, methodology, visualization,

writing – original draft. G. G.: Conceptualization, data curation, formal analysis, funding acquisition, investigation, methodology, project administration, validation, writing – original draft. V. L.: Formal analysis, investigation, validation, writing – review & editing. Y. P.: Formal analysis, investigation, validation, writing – review & editing. P. A.: Formal analysis, investigation, validation, writing – review & editing. A. ur R.: Investigation, writing – review & editing. N. R.: Project administration, resources, supervision, writing – review & editing. E. R.: Funding acquisition, project administration, resources, supervision, writing – review & editing. All the authors have approved the final manuscript.

Use of AI statement

None.

References

[1] Bogdanov, D.; Farfan, J.; Sadovskaia, K.; Aghahosseini, A.; Child, M.; Gulagi, A.; Solomon, O.; de Souza Noel Simas Barbosa, L.; Breyer, C. Radical transformation pathway towards sustainable electricity via evolutionary steps. *Nat. Commun.* **2019**, *10*, 1077.

[2] Haszeldine, R. S. Carbon capture and storage: How green can black be. *Science* **2009**, *325*, 1647–1652.

[3] Ishaq, M.; Ghouse, G.; Fernández-González, R.; Puime-Guillén, F.; Tandir, N.; Santos de Oliveira, H. M. From fossil energy to renewable energy: Why is circular economy needed in the energy transition. *Front. Environ. Sci.* **2022**, *10*, 941791.

[4] Geissdoerfer, M.; Savaget, P.; Bocken, N. M. P.; Hultink, E. J. The circular economy—A new sustainability paradigm. *J. Clean. Prod.* **2017**, *143*, 757–768.

[5] Daiyan, R.; MacGill, I.; Amal, R. Opportunities and challenges for renewable power-to-X. *ACS Energy Lett.* **2020**, *5*, 3843–3847.

[6] Vázquez, F. V.; Koponen, J.; Ruuskanen, V.; Bajamundi, C.; Kosonen, A.; Simell, P.; Ahola, J.; Frilund, C.; Elfving, J.; Reinikainen, M. et al. Power-to-X technology using renewable electricity and carbon dioxide from ambient air: SOLETAIR proof-of-concept and improved process concept. *J. CO_2 Util.* **2018**, *28*, 235–246.

[7] Ruuskanen, V.; Givirovskiy, G.; Elfving, J.; Kokkonen, P.; Karvinen, A.; Järvinen, L.; Sillman, J.; Vainikka, M.; Ahola, J. Neo-Carbon Food concept: A pilot-scale hybrid biological-inorganic system with direct air capture of carbon dioxide. *J. Clean. Prod.* **2021**, *278*, 123423.

[8] Ishaq, H.; Dincer, I.; Crawford, C. A review on hydrogen production and utilization: Challenges and opportunities. *Int. J. Hydrogen Energy* **2022**, *47*, 26238–26264.

[9] Ursúa, A.; Gandía, L. M.; Sanchis, P. Hydrogen production from water electrolysis: Current status and future trends. *Proc. IEEE* **2012**, *100*, 410–426.

[10] Suen, N. T.; Hung, S. F.; Quan, Q.; Zhang, N.; Xu, Y. J.; Chen, H. M. Electrocatalysis for the oxygen evolution reaction: Recent development and future perspectives. *Chem. Soc. Rev.* **2017**, *46*, 337–365.

[11] Jiao, Y.; Zheng, Y.; Jaroniec, M.; Qiao, S. Z. Design of electrocatalysts for oxygen- and hydrogen-involving energy conversion reactions. *Chem. Soc. Rev.* **2015**, *44*, 2060–2086.

[12] Givirovskiy, G.; Ruuskanen, V.; Kokkonen, P.; Karvinen, A.; Givirovskaia, D.; Repo, E.; Ahola, J. Pilot-scale *in situ* water electrolyzer with an improved fluid flow and modified electrodes for upscaling hybrid biological-inorganic systems. *J. Clean. Prod.* **2021**, *314*, 128001.

[13] Wang, S.; Lu, A. L.; Zhong, C. J. Hydrogen production from water electrolysis: Role of catalysts. *Nano Converg.* **2021**, *8*, 4.

[14] Seh, Z. W.; Kibsgaard, J.; Dickens, C. F.; Chorkendorff, I.; Nørskov, J. K.; Jaramillo, T. F. Combining theory and experiment in electrocatalysis: Insights into materials design. *Science* **2017**, *355*, eaad4998.

[15] Song, F.; Bai, L. C.; Moysiadou, A.; Lee, S.; Hu, C.; Liardet, L.; Hu, X. L. Transition metal oxides as electrocatalysts for the oxygen evolution reaction in alkaline solutions: An application-inspired renaissance. *J. Am. Chem. Soc.* **2018**, *140*, 7748–7759.

[16] Kumaravel, S.; Karthick, K.; Sankar, S. S.; Karmakar, A.; Madhu, R.; Bera, K.; Kundu, S. Current progressions in transition metal based hydroxides as bi-functional catalysts towards electrocatalytic total water splitting. *Sustain. Energy Fuels* **2021**, *5*, 6215–6268.

[17] Zhan, Y.; Lu, M. H.; Yang, S. L.; Xu, C. H.; Liu, Z. L.; Lee, J. Y. Activity of transition-metal (manganese, iron, cobalt, and nickel) phosphates for oxygen electrocatalysis in Alkaline Solution. *ChemCatChem* **2016**, *8*, 372–379.

[18] Gupta, S.; Patel, M. K.; Miotello, A.; Patel, N. Metal boride-based catalysts for electrochemical water-splitting: A review. *Adv. Funct. Mater.* **2020**, *30*, 1906481.

[19] Su, H.; Jiang, J.; Song, S. J.; An, B. H.; Li, N.; Gao, Y. Q.; Ge, L. Recent progress on design and applications of transition metal chalcogenide-associated electrocatalysts for the overall water splitting. *Chin. J. Catal.* **2023**, *44*, 7–49.

[20] Jiao, L.; Seow, J. Y. R.; Skinner, W. S.; Wang, Z. U.; Jiang, H. L. Metal-organic frameworks: Structures and functional applications. *Mater. Today* **2019**, *27*, 43–68.

[21] Givirovskaia, D.; Givirovskiy, G.; Haapakoski, M.; Hokkanen, S.; Ruuskanen, V.; Salo, S.; Marjomäki, V.; Ahola, J.; Repo, E. Modification of face masks with zeolite imidazolate framework-8: A tool for hindering the spread of COVID-19 infection. *Microporous Mesoporous Mater.* **2022**, *334*, 111760.

[22] Cui, Y. J.; Li, B.; He, H. J.; Zhou, W.; Chen, B. L.; Qian, G. D. Metal-organic frameworks as platforms for functional materials. *Acc. Chem. Res.* **2016**, *49*, 483–493.

[23] Zheng, W. R.; Lee, L. Y. S. Metal-organic frameworks for electrocatalysis: Catalyst or precatalyst. *ACS Energy Lett.* **2021**, *6*, 2838–2843.

[24] Zhou, J.; Dou, Y. B.; Zhou, A. W.; Guo, R. M.; Zhao, M. J.; Li, J. R. MOF template-directed fabrication of hierarchically structured electrocatalysts for efficient oxygen evolution reaction. *Adv. Energy Mater.* **2017**, *7*, 1602643.

[25] Cai, G. R.; Zhang, W.; Jiao, L.; Yu, S. H.; Jiang, H. L. Template-directed growth of well-aligned mof arrays and derived self-supporting electrodes for water splitting. *Chem* **2017**, *2*, 791–802.

[26] Sun, Y. J.; Zhou, H. C. Recent progress in the synthesis of metal-organic frameworks. *Sci. Technol. Adv. Mater.* **2015**, *16*, 054202.

[27] Zhu, Y. J.; Chen, F. Microwave-assisted preparation of inorganic nanostructures in liquid phase. *Chem. Rev.* **2014**, *114*, 6462–6555.

[28] Thomas-Hillman, I.; Laybourn, A.; Dodds, C.; Kingman, S. W. Realising the environmental benefits of metal-organic frameworks: Recent advances in microwave synthesis. *J. Mater. Chem. A* **2018**, *6*, 11564–11581.

[29] Kumar, A.; Kuang, Y.; Liang, Z.; Sun, X. M. Microwave chemistry, recent advancements, and eco-friendly microwave-assisted synthesis of nanoarchitectures and their applications: A review. *Mater. Today Nano* **2020**, *11*, 100076.

[30] Chen, C. W.; Feng, X. B.; Zhu, Q.; Dong, R.; Yang, R.; Cheng, Y.; He, C. Microwave-assisted rapid synthesis of well-shaped MOF-74 (Ni) for CO_2 efficient capture. *Inorg. Chem.* **2019**, *58*, 2717–2728.

[31] Vakili, R.; Xu, S. J.; Al-Janabi, N.; Gorgojo, P.; Holmes, S. M.; Fan, X. L. Microwave-assisted synthesis of zirconium-based metal organic frameworks (MOFs): Optimization and gas adsorption. *Microporous Mesoporous Mater.* **2018**, *260*, 45–53.

[32] Zhong, M.; Kong, L. J.; Zhao, K.; Zhang, Y. H.; Li, N.; Bu, X. H. Recent progress of nanoscale metal-organic frameworks in synthesis and battery applications. *Adv. Sci.* **2021**, *8*, 2001980.

[33] Zhang, B.; Zheng, Y. J.; Ma, T.; Yang, C. D.; Peng, Y. F.; Zhou, Z. H.; Zhou, M.; Li, S.; Wang, Y. H.; Cheng, C. Designing MOF

nanoarchitectures for electrochemical water splitting. *Adv. Mater.* **2021**, *33*, 2006042.
[34] Lux, L.; Williams, K.; Ma, S. Q. Heat-treatment of metal-organic frameworks for green energy applications. *CrystEngComm* **2015**, *17*, 10–22.
[35] Alli, R. D.; Zhou, R. F.; Mohamedali, M.; Mahinpey, N. Effect of thermal treatment conditions on the stability of MOF-derived Ni/CeO_2 catalyst for dry reforming of methane. *Chem. Eng. J.* **2023**, *466*, 143242.
[36] Guo, S. L.; Gao, M.; Zhang, W.; Liu, F.; Guo, X. Y.; Zhou, K. Recent advances in laser-induced synthesis of MOF derivatives. *Adv. Mater.* **2023**, *35*, 2303065.
[37] Tang, Y. J.; Zheng, H.; Wang, Y.; Zhang, W.; Zhou, K. Laser-induced annealing of metal-organic frameworks on conductive substrates for electrochemical water splitting. *Adv. Funct. Mater.* **2021**, *31*, 2102648.
[38] Yan, W.; Jiang, H. Q.; Yi, W. D.; Zhao, C. B.; Xia, Y. C.; Cong, H. J.; Tang, L.; Cheng, G. J.; He, J. H.; Deng, H. X. High-entropy-alloy nanoparticles synthesized by laser metallurgy using a multivariate MOF. *Mater. Chem. Front.* **2022**, *6*, 2796–2802.
[39] Kawashima, K.; Márquez, R. A.; Son, Y. J.; Guo, C.; Vaidyula, R. R.; Smith, L. A.; Chukwuneke, C. E.; Mullins, C. B. Accurate potentials of Hg/HgO electrodes: Practical parameters for reporting alkaline water electrolysis overpotentials. *ACS Catal.* **2023**, *13*, 1893–1898.
[40] Aykut, Y.; Bayrakçeken Yurtcan, A. Nanostructured electrocatalysts for low-temperature water splitting: A review. *Electrochim. Acta* **2023**, *471*, 143335.
[41] Yi, X. R.; Sun, H. P.; Robertson, N.; Kirk, C. Nanoflower $Ni(OH)_2$ grown *in situ* on Ni foam for high-performance supercapacitor electrode materials. *Sustain. Energy Fuels* **2021**, *5*, 5236–5246.
[42] Cao, J.; Zhang, Z. J.; Li, H. C.; Zhu, R. T.; Li, S. B.; Ma, L.; Zhou, K. C.; Wei, Q. P.; Luo, F. H. Facile preparation of nickel hydroxide nanoplates on nickel foam for high performance hydrogen generation. *Sustain. Energy Fuels* **2020**, *4*, 5031–5035.
[43] Nakatsuka, K.; Yoshii, T.; Kuwahara, Y.; Mori, K.; Yamashita, H. Controlled pyrolysis of Ni-MOF-74 as a promising precursor for the creation of highly active Ni nanocatalysts in size-selective hydrogenation. *Chem.—Eur. J.* **2018**, *24*, 898–905.
[44] Chen, S. R.; Xue, M.; Li, Y. Q.; Pan, Y.; Zhu, L. K.; Qiu, S. L. Rational design and synthesis of $Ni_xCo_{3-x}O_4$ nanoparticles derived from multivariate MOF-74 for supercapacitors. *J. Mater. Chem. A* **2015**, *3*, 20145–20152.
[45] Du, X. Q.; Yang, Z.; Li, Y.; Gong, Y. Q.; Zhao, M. Controlled synthesis of $Ni(OH)_2/Ni_3S_2$ hybrid nanosheet arrays as highly active and stable electrocatalysts for water splitting. *J. Mater. Chem. A* **2018**, *6*, 6938–6946.
[46] Xie, S. Z.; Qin, Q. J.; Liu, H.; Jin, L. J.; Wei, X. L.; Liu, J. X.; Liu, X.; Yao, Y. C.; Dong, L. H.; Li, B. MOF-74-M (M = Mn, Co, Ni, Zn, MnCo, MnNi, and MnZn) for low-temperature NH_3-SCR and *in situ* DRIFTS study reaction mechanism. *ACS Appl. Mater. Interfaces* **2020**, *12*, 48476–48485.
[47] Halder, M.; Islam, M.; Singh, P.; Singha Roy, A.; Islam, S. M.; Sen, K. Sustainable generation of $Ni(OH)_2$ nanoparticles for the green synthesis of 5-substituted 1H-tetrazoles: A competent turn on fluorescence sensing of H_2O_2. *ACS Omega* **2018**, *3*, 8169–8180.
[48] Hayat, A.; Mane, S. K. B.; Shaishta, N.; Khan, J.; Hayat, A.; Keyum, G.; Uddin, I.; Raziq, F.; Khan, M.; Manjunatha, G. Nickel oxide nanoparticles on 3D nickel foam substrate as a non-enzymatic glucose sensor. *J. Electrochem. Soc.* **2019**, *166*, B1602–B1611.
[49] Gogoi, P.; Saikia, B. J.; Dolui, S. K. Effects of Nickel Oxide (NiO) nanoparticles on the performance characteristics of the jatropha oil based alkyd and epoxy blends. *J. Appl. Polym. Sci.* **2015**, *132*, 41490.
[50] Zhou, J. J.; Ji, W. X.; Xu, L.; Yang, Y.; Wang, W. Q.; Ding, H. L.; Xu, X. C.; Wang, W. W.; Zhang, P. L.; Hua, Z. L. et al. Controllable transformation of CoNi-MOF-74 on Ni foam into hierarchical-porous $Co(OH)_2/Ni(OH)_2$ micro-rods with ultra-high specific surface area for energy storage. *Chem. Eng. J.* **2022**, *428*, 132123.
[51] Dubey, P.; Kaurav, N.; Devan, R. S.; Okram, G. S.; Kuo, Y. K. The effect of stoichiometry on the structural, thermal and electronic properties of thermally decomposed nickel oxide. *RSC Adv.* **2018**, *8*, 5882–5890.
[52] Payne, B. P.; Biesinger, M. C.; McIntyre, N. S. Use of oxygen/nickel ratios in the XPS characterisation of oxide phases on nickel metal and nickel alloy surfaces. *J. Electron Spectros. Relat. Phenomena* **2012**, *185*, 159–166.
[53] Liu, Q. Q.; Yue, K. F.; Weng, X. J.; Wang, Y. Y. Luminescence sensing and supercapacitor performances of a new (3,3)-connected Cd-MOF. *CrystEngComm* **2019**, *21*, 6186–6195.
[54] Wang, X.; Liu, J. Y.; Wang, Y. Y.; Zhao, C. M.; Zheng, W. T. $Ni(OH)_2$ nanoflakes electrodeposited on Ni foam-supported vertically oriented graphene nanosheets for application in asymmetric supercapacitors. *Mater. Res. Bull.* **2014**, *52*, 89–95.
[55] Milazzo, R. G.; Privitera, S. M. S.; Scalese, S.; Monforte, F.; Bongiorno, C.; Condorelli, G. G.; Lombardo, S. A. Ultralow loading electroless deposition of IrO_x on nickel foam for efficient and stable water oxidation catalysis. *Int. J. Hydrogen Energy* **2020**, *45*, 26583–26594.
[56] Liu, J. L.; Wang, Z. Y.; Su, K. D.; Xv, D.; Zhao, D.; Li, J. H.; Tong, H. X.; Qian, D.; Yang, C. M.; Lu, Z. G. Self-supported hierarchical IrO_2@NiO nanoflake arrays as an efficient and durable catalyst for electrochemical oxygen evolution. *ACS Appl. Mater. Interfaces* **2019**, *11*, 25854–25862.
[57] Sun, C. C.; Dong, Q. C.; Yang, J.; Dai, Z. Y.; Lin, J. J.; Chen, P.; Huang, W.; Dong, X. C. Metal-organic framework derived $CoSe_2$ nanoparticles anchored on carbon fibers as bifunctional electrocatalysts for efficient overall water splitting. *Nano Res.* **2016**, *9*, 2234–2243.
[58] Qin, F.; Zhao, Z. H.; Alam, K.; Ni, Y. Z.; Robles-Hernandez, F.; Yu, L.; Chen, S.; Ren, Z. F.; Wang, Z. M.; Bao, J. M. Trimetallic NiFeMo for overall electrochemical water splitting with a low cell voltage. *ACS Energy Lett.* **2018**, *3*, 546–554.
[59] Lin, Y. P.; Wang, H.; Peng, C. K.; Bu, L. M.; Chiang, C. L.; Tian, K.; Zhao, Y.; Zhao, J. Q.; Lin, Y. G.; Lee, J. M. et al. Co-induced electronic optimization of hierarchical NiFe LDH for oxygen evolution. *Small* **2020**, *16*, 2002426.
[60] Ge, J.; Zhang, W.; Tu, J.; Xia, T.; Chen, S. P.; Xie, G. Suppressed Jahn–teller distortion in $MnCo_2O_4$@Ni_2P heterostructures to promote the overall water splitting. *Small* **2020**, *16*, 2001856.
[61] Reier, T.; Oezaslan, M.; Strasser, P. Electrocatalytic oxygen evolution reaction (OER) on Ru, Ir, and Pt catalysts: A comparative study of nanoparticles and bulk materials. *ACS Catal.* **2012**, *2*, 1765–1772.
[62] Givirovskiy, G.; Ruuskanen, V.; Väkiparta, T.; Ahola, J. Electrocatalytic performance and cell voltage characteristics of 1st-row transition metal phosphate (TM-Pi) catalysts at neutral pH. *Mater. Today Energy* **2020**, *17*, 100426.